

Ten implementations of ptychography

PENG LI  & ANDREW M. MAIDEN

Department of Electronic and Electrical Engineering, University of Sheffield, Sheffield, UK

Key words. Diffuser, phase retrieval, ptychography.

Summary

Ptychography is an increasingly popular phase retrieval imaging technique, able to routinely deliver quantitative phase images with extended field of view at diffraction limited resolution. Different variants of this technique, like Bragg ptychography and Fourier ptychography, have also been developed and applied to various fields. Here we experimentally demonstrate 10 ways to implement the conventional real space transmission ptychography, and compare their properties to provide a guide to choosing the optimal setup for a specific application.

Introduction

When it was first proposed as a lensless imaging alternative for electron microscopy in the 1970s (Hoppe, 1969a,b; Hoppe & Strube, 1969; Hegerl & Hoppe, 1970, 1972), ptychography could only be applied to crystalline objects, thanks to the constrained set of interference phenomena that can occur in this case. It was not until 1989 when Bates and Rodenburg proposed a direct (noniterative) reconstruction algorithm called the Wigner distribution deconvolution method (WDDM) (Bates & Rodenburg, 1989), that ptychography became applicable to amorphous objects. However, WDDM still requires the specimen to be scanned over a grid of 2D positions separated by the desired resolution in the final reconstruction and a 2D diffraction intensity to be recorded at each scan position, which gives rise to a very large 4D data set. The 4D data set, however, can be substantially reduced by using fewer and bigger detector pixels when the sample satisfies the weak phase approximation (McCallum *et al.*, 1995; Yang *et al.*, 2015; Brown *et al.*, 2016). A breakthrough in ptychography was made when iterative algorithms were used to solve for the phase problem in 2004 (Faulkner & Rodenburg, 2004; Rodenburg & Faulkner, 2004). Since then, further algorithmic developments have made ptychography a very powerful and useful imaging technique. Alongside the object function, the illumination function (Guizar-Sicairos & Fienup, 2008; Maiden & Rodenburg, 2009; Thibault *et al.*, 2009), the scan

positions (Maiden *et al.*, 2012a; Zhang *et al.*, 2013; Tripathi *et al.*, 2014) and the partial coherence (Thibault & Menzel, 2013) can also be recovered from the dataset. In addition, ptychography can image 3D objects via the multislice method (Maiden *et al.*, 2012b) or via the combination of tomography (Dierolf *et al.*, 2010). It has also been modified to operate in a Bragg geometry (Godard *et al.*, 2011) and adapted to eliminate the mechanical scan of the specimen via Fourier Ptychography (Zheng *et al.*, 2013) where the roles of real and reciprocal space are interchanged and the ‘scanning’ is carried out by illumination tilts.

The ptychographic imaging process is illustrated in Figure 1(A). There are three fundamental components: a confined probe, an overlapping scan strategy and an iterative image reconstruction algorithm. The confined probe can be formed by passing an extended beam through a pinhole or by condensing the extended beam via a lens. In either case, a diffuser (a randomly scattering medium) can also be inserted to increase the angular range of the probe, giving rise to the four probe-forming methods illustrated in Figure 1(B). (In what follows, the four methods will be referred to according to their numbering in Fig. 1B.) It should be noted that although a probe can also be formed by imaging a pinhole (or a pinhole with a diffuser) via a 4f system (Maiden *et al.*, 2012b), this is essentially the same as probe 3 (or probe 4) in Figure 1(B).

Ptychography makes measurements of multiple diffraction patterns via an overlapping scan strategy, where the illuminated areas from two adjacent scan positions partially overlap. Provided this overlap is sufficient, the redundancy it introduces allows iterative algorithms to re-phase the measurements and reconstruct complex images of the specimen and the probe. These algorithms broadly follow the block diagram shown in Figure 1(C), although there are many variants on how each block in the diagram is implemented; we will use the ePIE algorithm (Maiden & Rodenburg, 2009) throughout this paper.

Although invented to circumvent the need for lenses, ptychography can also be implemented with their assistance. There are three possible setups (the variant Fourier ptychography is not considered here). We will refer to the configuration with no lenses in between the specimen and the detector as the ‘lensless setup’ (see Fig. 2A). This is the most common form of ptychography and it is very popular in the x-ray

Correspondence to: Peng Li, Department of Electronic and Electrical Engineering, University of Sheffield, Sheffield, UK, S1 3JD. Tel: 0114 222 5181; E-mail: peng.li.shef@sheffield.ac.uk

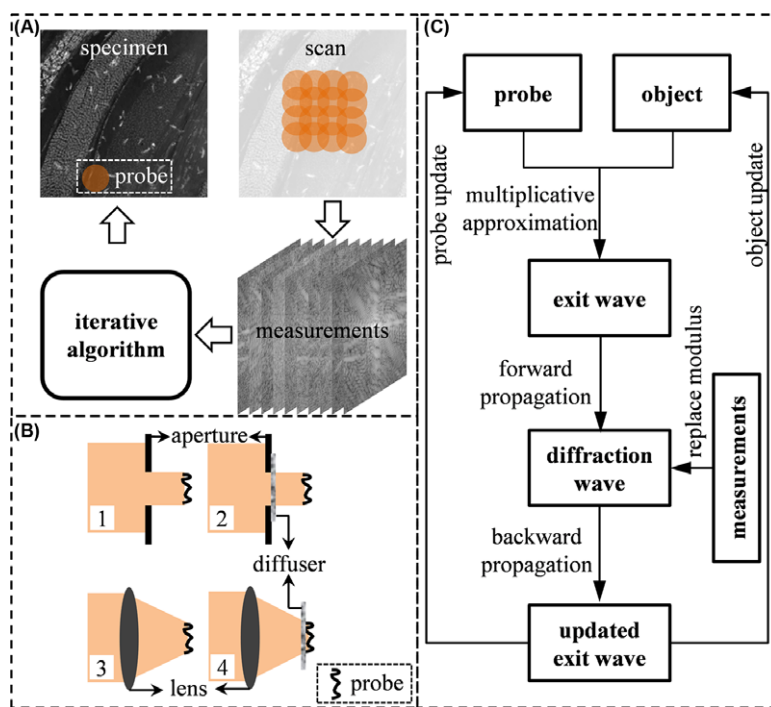


Fig. 1. Ptychographic imaging. (A) The flow chart of ptychographic imaging. (B) The experimental geometries to form a localised probe in ptychography. (C) The block diagram of a typical iterative reconstruction algorithm in ptychography.

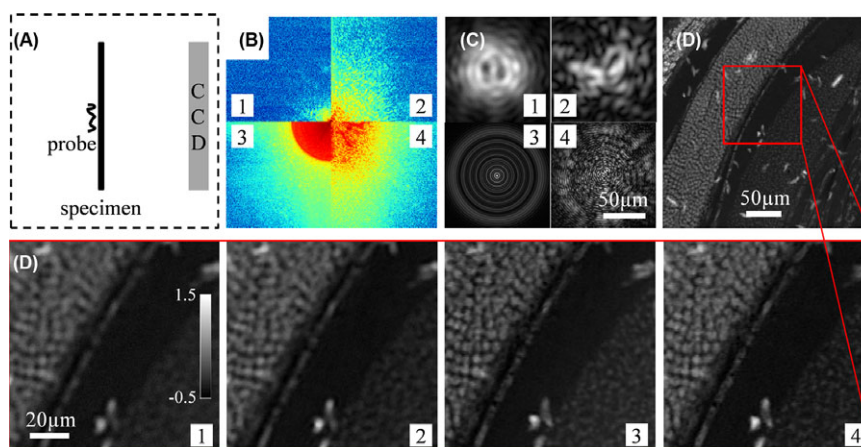


Fig. 2. The lensless setup of ptychography. (A) Experimental configuration. The probe can be formed by any way of the four shown in Figure 1(B). (B) Example diffraction patterns from the four probe-forming optics. (C) The four probe reconstructions. (D) The phase part of the specimen reconstruction. (E) The zoom-ins of the specimen phase reconstructions from the four different probe-forming optics.

community (Thibault *et al.*, 2008). An alternative configuration using a microscope imaging system (an objective lens and a tube lens) to image near-field diffraction patterns has been demonstrated in the visible light regime (Godden *et al.*, 2014); we refer to this setup as the ‘microscope setup’ because of its similar appearance to a microscope. Another approach is the ‘selected area setup’, which has been demonstrated using visible light (Maiden *et al.*, 2010) and also in electron microscopy (Maiden *et al.*, 2015), where the objective lens

images the specimen onto a selected area aperture and the resulting wavefront forms a near-field diffraction pattern on a detector. Compared to the lensless setup, in the microscope setup the detector is replaced with its demagnified image (see Fig. 4A) and in the selected area setup the specimen is replaced with its magnified image (see Fig. 7A).

Combined with the four probe types, the three imaging setups can give rise to 10 ways to implement ptychography (because for the selected area setup, plane wave illumination

is needed, so probes 3 and 4 cannot be used). Our objectives in this paper are to demonstrate these 10 different configurations using visible light experiments, to compare their performance, and to assess the advantages and disadvantages of each approach.

Experiments

For each of the 10 different configurations, we carried out a ptychographic experiment on a microscope slide of moss antheridium (see Fig. 2D) using a 635 nm laser diode source. For each experiment, the ptychographic scans consisted of a 15×15 raster grid of specimen positions with a nominal $20 \mu\text{m}$ step size, plus $\pm 20\%$ random offsets to the grid to avoid reconstruction artefacts. In the experiments, the aperture used to form probe types 1 and 2 had a diameter of $100 \mu\text{m}$ and the lens chosen to form probe 3 and probe 4 had a focal length of 35 mm . The NA of the lens was about 0.17. The diffuser used in probe 2 and probe 4 was a piece of plastic film. The 16-bit CCD detector used to record the diffraction patterns had 2048×2048 pixels with a pitch of $7.4 \mu\text{m}^2$. The recorded diffraction patterns were binned by a factor of 2 to save data processing time and reduce noise.

The lensless setup

The lensless setup is illustrated in Figure 2(A). The distance from the specimen to the detector was set at 17 mm , resulting in a pixel size for the reconstructed specimen image approximately matching the experiments using the other setups. The diffraction patterns that resulted from the four different probes (at the central scan position) are shown in Figure 2(B). As we can see, the aperture on its own (probe 1) produces a bright spot in the centre of the diffraction pattern caused by the unscattered beam. As a result, the scattered beam, especially at high angles, is too weak to be detected with good signal-to-noise ratio because of the limited dynamic range of the CCD. The use of a diffuser or a lens can help mitigate this problem by introducing higher incident angles into the probe illumination. In this case, on comparing the top right and bottom left diffraction patterns in Figure 2(B), the higher intensities toward the edges of the bottom left diffraction pattern indicate that the lens introduces a greater range of angles than does the diffuser. When the diffuser and the lens are used together, a much broader region of the CCD can detect significant signals. As a result, this allows us to expect the worst reconstruction from probe 1 and best reconstruction from probe 4.

We used the Fresnel number (Goodman, 2005) as the criteria to determine the propagation model between the specimen and the detector. The Fresnel number is defined as

$$N_F = \frac{a^2}{\lambda z}, \quad (1)$$

where a is the size of the probe, λ the wavelength of the radiation source and z the distance of the detector from the specimen. When $N_F \ll 1$, the Fourier propagation (i.e. Fraunhofer diffraction) should be used; when $N_F \approx 1$, the Fresnel propagation (i.e. Fresnel diffraction) should be used; and when $N_F \gg 1$, the angular spectrum propagation should be used. Here the Fresnel number is approximately 0.93, very close to 1, so we used the Fresnel propagation in the reconstruction. The Fresnel propagation model is given by

$$\Psi(u, v) = FT \left\{ \psi(x, y) \exp \left[\frac{i\pi}{\lambda z} (x^2 + y^2) \right] \right\}, \quad (2)$$

where (x, y) is the coordinate of the specimen plane, (u, v) the coordinate of the detector plane and FT is the Fourier transform operation. The pixel dimensions $(\Delta x, \Delta y)$ in the specimen plane are given by

$$\begin{cases} \Delta x = \frac{\lambda z}{D_x} \\ \Delta y = \frac{\lambda z}{D_y} \end{cases}, \quad (3)$$

where D_x and D_y are the detector dimension along the x and y directions, respectively. Here the pixel size of the reconstructions is about $0.71 \mu\text{m}$ in each direction.

A total of 200 iterations of ePIE were run on each data set. The initial object guess was free space, that is, a matrix of 1 s. The initial probe guess was generated according to the experimental geometry: for probe 1 and probe 2, the initial guess was just an aperture of approximately the correct size; for probe 3 and probe 4, the initial guess was a modelled convergent beam with a defocus applied to match that measured from the experimental apparatus. The moduli of the reconstructed probes from each of the four probe types are shown in Figure 2(C). Figure 2(D) gives the full reconstructed image from the experiment using probe 4 as an example, whereas Figure 2(E) shows zoom-ins of the four object reconstructions from each of the four probe types.

Visually, the reconstruction quality is consistent with the above analysis of the recorded diffraction patterns, with probes 3 and 4 giving much sharper features. To quantitatively assess the reconstruction quality, we used a metric called Fourier ring correlation (FRC) (Van Heel & Schatz, 2005). The FRC calculates the frequency correlation between the results from two independent experiments. High correlation means the information of the corresponding frequency is stably reconstructed, whereas low correlation implies the information is not reliable. The FRC plot is shown in Figure 3 and it indicates the same quality trend as that of the visual comparison.

The microscope setup

The microscope setup, where diffraction data is collected using a conventional microscope followed by a CCD detector, is illustrated in Figure 4(A). Here the microscope used an

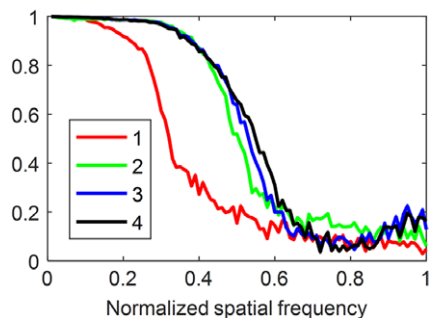


Fig. 3. FRC curves comparison for the lensless setup.

objective lens with a NA of 0.65 combined with a tube lens of focal length 100 mm, giving a calibrated magnification for our system of 21.45. Ignoring lens aberrations, this setup can be viewed equivalently as a lensless setup with a very small virtual CCD, demagnified by the microscope magnification and located at the front focal plane of the objective lens. Because the CCD is much smaller now, the distance from the specimen to the CCD conjugate plane cannot be too big, otherwise signals will be scattered beyond the edges of the virtual detector. Here we set this distance to be 0.5 mm, giving diffraction patterns as shown in Figure 4(B). It should be noted that because the virtual CCD plane is at the proximity of the specimen plane, the resulting diffraction patterns will have a relatively low dynamic range compared to the lensless setup. As a result, the dynamic range of the detector is not a limiting factor anymore and the signals can be detected with high fidelity for all the four probe-forming methods. Consequently, it is difficult to predict the reconstruction quality here based solely on the diffraction patterns themselves.

For the reconstruction, the CCD was scaled down to its conjugate plane, which means the detector is demagnified by 21.45. According to the Fresnel number calculation (about

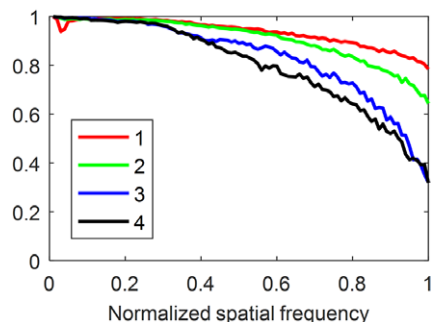


Fig. 5. FRC curves comparison for the microscope setup.

31.5, much bigger than 1), the angular spectrum propagation model is used for the propagation between the specimen and the CCD conjugate plane. The angular spectrum propagation model is given by

$$\begin{aligned} \psi'(x, y) = & FT^{-1} \left\{ FT \{ \psi(x, y) \} \right. \\ & \times \exp \left[\frac{i 2 \pi z}{\lambda} \sqrt{1 - (\lambda u)^2 - (\lambda v)^2} \right] \\ & \left. \times \text{circ} \left(\sqrt{(\lambda u)^2 + (\lambda v)^2} \right) \right\}, \end{aligned} \quad (4)$$

with

$$\text{circ} \left(\sqrt{(\lambda u)^2 + (\lambda v)^2} \right) = \begin{cases} 1, & (\lambda u)^2 + (\lambda v)^2 \leq 1 \\ 0, & (\lambda u)^2 + (\lambda v)^2 > 1 \end{cases}, \quad (5)$$

where FT^{-1} is the inverse Fourier transform operation. The pixel size of the specimen and the pixel size of the virtual detector are equal because of the two successive Fourier transforms in the angular spectrum propagator. Because the virtual detector is formed by demagnifying the actual detector by 21.45,

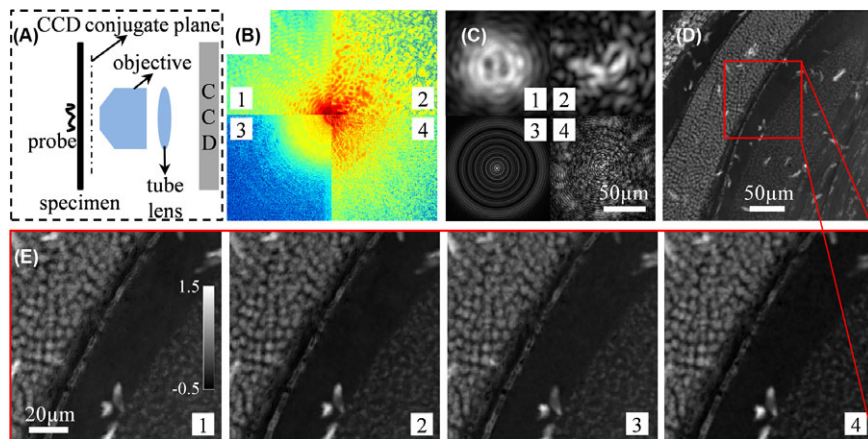


Fig. 4. The microscope setup of ptychography. (A) Experimental configuration. The probe can be formed by any way of the four shown in Figure 1(B). (B) Example diffraction patterns from the four probe-forming optics. (C) The four probe reconstructions. (D) The phase part of the specimen reconstruction. (E) The zoomins of the specimen phase reconstructions from the four different probe-forming optics.

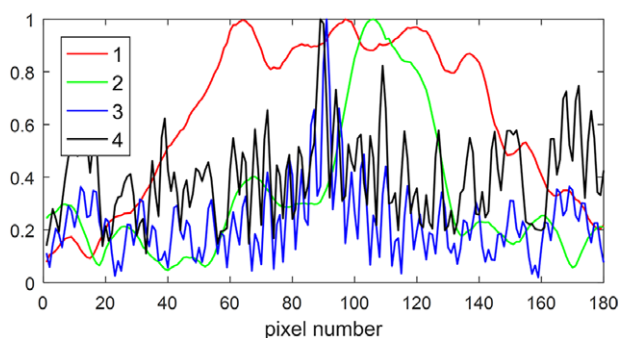


Fig. 6. The cross-section plots of the four probes shown in Figure 4(C) along the central vertical line.

the pixel size of the reconstructions is equal to $2 \times 7.4/21.45 = 0.69 \mu\text{m}$.

As previously, 200 iterations of ePIE were run on each data set with an initial object guess of free space and an initial probe guess being generated according to the experimental geometry. The reconstructed probes (the modulus part of the central region with significant values) from each of the four probe types are shown in Figure 4(C). Figure 4(D) gives the full reconstructed image from the experiment using probe 4 as an example, whereas Figure 4(E) shows zoom-ins of the four object reconstructions from each of the four probe types.

Visually, compared to the results from the lensless setup, the four reconstructions are all very good. Quantitatively, an FRC analysis gives very high correlations for all the methods (see Fig. 5), compared to those from the lensless setup. But surprisingly, the reconstruction quality trend is opposite to the case

of the lensless setup. Because the recorded diffraction patterns all have good enough signal-to-noise ratios, we suspect that the reconstruction quality is more affected by the structure of the probe here. The specimen reconstruction is realised by decoupling the probe from the updated exit wave (see Fig. 1C), meaning the probe structure and the specimen reconstruction are interdependent. If the probe structure is very rough, it will cause similar profile variations in the specimen reconstruction, hence affecting the FRC curve. As shown in Figure 4(C), probe 1 and 2 have rather smooth speckles with big characteristic size, whereas probe 3 has a bright spot in the centre and ripples, and probe 4 has very small and random speckles. It is obvious, when we plot their cross-sections along the central vertical line in Figure 6, to see that probe 1 and 2 have much more smooth profiles compared to probe 3 and 4. To quantitatively compare the profile smoothness of the four probes, we adopt a quantity called the total variation (Rudin *et al.*, 1992) as defined by

$$V(P) = \sum_{x,y} \sqrt{|P_{x+1,y} - P_{x,y}|^2 + |P_{x,y+1} - P_{x,y}|^2}, \quad (6)$$

where $V(P)$ is the total variation of probe P , and xy are the pixel indices along the two dimensions of the probe. The lower the number is, the less variation, that is more smooth, the probe profile is. The total variations for the four probes are calculated to be 0.96×10^3 , 1.6×10^3 , 2.4×10^3 and 5.0×10^3 , respectively, which is consistent with the FRC comparison. Moreover, the oscillating nature of the FRCs at high frequencies from probe 3 and 4 also proves that the specimen reconstructions have unstable high frequencies.

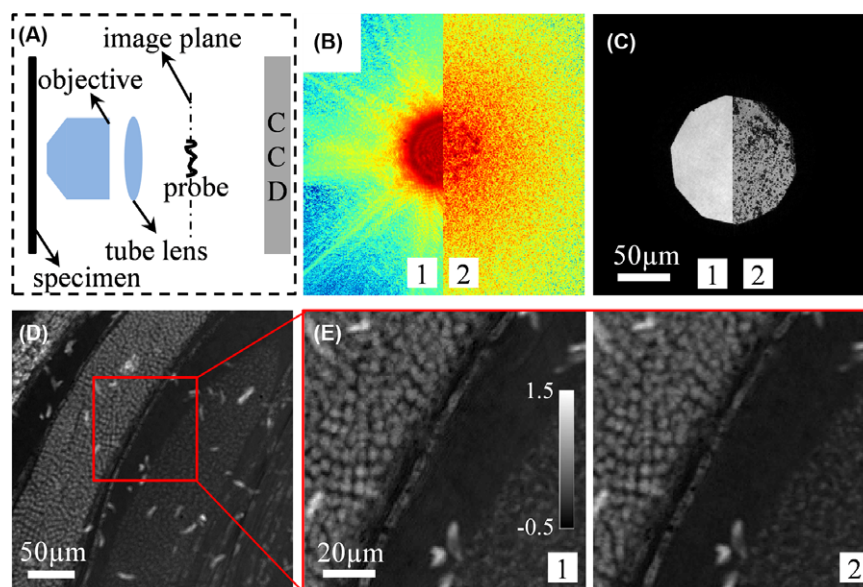


Fig. 7. The selected area setup of ptychography. (A) Experimental configuration. The probe can only be formed by the first two ways shown in Figure 1(B). (B) Example diffraction patterns from the two probe-forming optics. (C) The two probe reconstructions. (D) The phase part of the specimen reconstruction. (E) The zoomins of the specimen phase reconstructions from the two probe-forming optics.

The selected area setup

A microscope imaging system can be used to image the specimen onto an aperture (or an aperture plus a diffuser) which plays the role of the probe; when the sample is scanned, its image moves relative to the aperture. An illustration of the setup is shown in Figure 7(A). The aperture was set to have a diameter of 2.3 mm, so that the probe formed at the specimen plane has a size of $107\ \mu\text{m}$, to match the probe size of the previous experiments. The detector was placed at 250 mm downstream of the aperture, where a well-developed diffraction pattern can cover most of the detector. Examples of the recorded diffraction patterns from probe 1 and probe 2 are, respectively, shown in Figure 7(B). As we mentioned above, plane wave illumination is preferred to form an image of the specimen, so only probe 1 and probe 2 are demonstrated for this setup. The reconstruction was performed at the image plane, which means the object reconstruction needs to be demagnified by 21.45 to give the right scale. Again, according to the Fresnel number calculation (about 33.3, much bigger than 1), the reconstruction used the angular spectrum propagator for the propagation between the aperture plane and the detector plane. A total of 200 iterations of ePIE were run on each data set with object initial guess being free space and probe initial guess being an aperture (for both the diffused and undiffused probes). The reconstructed probes (modulus part) and the reconstructed object (phase part) from probe 2 are, respectively, shown in Figures 7(C) and 7(D) (the reconstructions are rescaled to the specimen plane). It should be noticed here that the object reconstructions are normally out-of-focused, due to the fact that the aperture was not exactly placed on the image plane. Therefore, an extra step of computational propagation is needed to bring the object reconstructions into focus. A zoom-in region of the in-focus object reconstructions are shown in Figure 7(E). Visually, the results are very good and comparable with that from the microscope setup. Likewise, FRC is calculated to quantitatively assess the image quality (see Fig. 8). Because the diffraction patterns are also measured at the proximity of the specimen image plane, for the same reason described above in the microscope setup section, probe 1 produces better object reconstruction than probe 2.

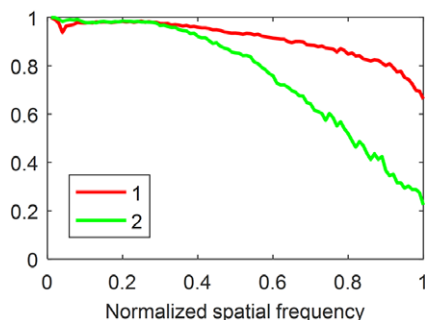


Fig. 8. FRC curves comparison for the selected area setup.

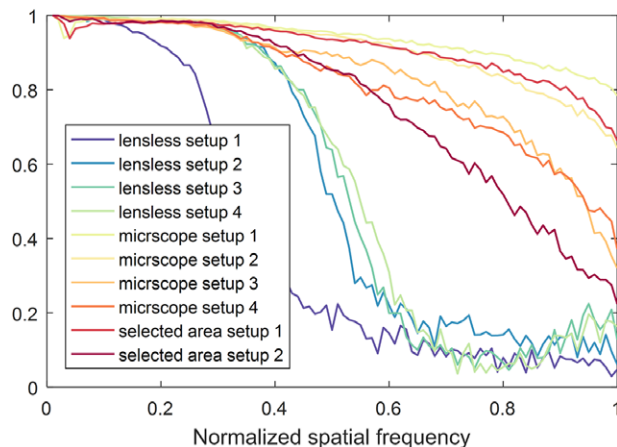


Fig. 9. FRC curves comparison for all the 10 implementations.

Discussions and conclusions

Here we have optically demonstrated 10 ways to implement ptychography using three different setups. The comparisons have been conducted among each setup. Because we have used the same sample, an overall comparison of all the 10 implementations using the FRC curves of the specimen reconstructions can be carried out and it is given in Figure 9. The best reconstruction is produced by the pinhole probe in the microscope setup, whereas the worst reconstruction results from the pinhole probe in the lensless setup. Although this comparison is restricted to the specific experiments in this work, for the generic case, we can draw two inferences. First, it is preferable to spread the diffraction pattern using either a lens or a diffuser because this reduces the dynamic range of the data and therefore makes it easier to record. Second, a diverse data set (obtained by using a diffuser) better conditions the reconstruction problem, but this comes with the caveat that a highly speckled probe (i.e. one with a high total variation) can reduce the accuracy of the reconstruction, because here it is possible that some regions of the object may never be well illuminated by the probe.

For the lensless setup, the diffraction pattern is measured at a relatively large distance from the specimen, where Fresnel or Fourier propagation models can be used. In this case, the requirement on the dynamic range of the detector is high, so that the signals scattered to high angles can be measured with high fidelity against the noise. This is problematic for weakly scattering samples, but using a diffuser or a condenser lens can significantly improve the situation. The long working distance that the lensless setup allows is its principle benefit, it is also the simplest setup and the cheapest. These benefits are offset by practical considerations, for instance the recorded diffraction patterns normally bear no relation to the profile of the specimen, so it is difficult to locate a region of interest, and accurate measurement of the distance from the specimen to the detector is a time consuming necessary step.

For the microscope setup, the diffraction pattern is measured at the vicinity of the virtual detector plane (i.e. the CCD conjugate plane, firmly in the near field). As a result, the dynamic range of the detector has only a minor influence on the reconstruction quality and the main limiting factor becomes the objective lens. When equipped with objectives of high quality and high NA, this setup produces good results just with a pinhole probe. But of course, good objectives are expensive. During the alignment, the specimen first coincides the virtual detector plane, so it is easy to locate the region of interest. Then, the specimen is defocused by moving the stage axially by a controllable distance, so the distance from the specimen to the measurement plane is known accurately. However, setting this distance too large reduces the NA of the system, so the working distance is quite limited.

For the selected area setup, the object reconstruction is the complex wave field in the selected area aperture plane. Only when the image plane coincides perfectly with the aperture plane is the specimen reconstruction in focus, otherwise a computational propagation is needed after the reconstruction to bring the specimen to focus. Because this setup compresses the specimen information into a 2D complex wave, it is very useful when the 3D scattering inside the specimen renders the multiplicative approximation on which the other methods rely inaccurate – an example of this is optical metrology for contact lenses or optics characterisation (Moore & Fienup, 2016).

For visible light, an advantage of the microscope setup is its compatibility with existing microscope platforms – a commercial microscope can be easily modified by adding a translational stage to implement ptychographic experiments. In this way, the resolution is still determined by the transfer function of the imaging system, but quantitative phase images can be obtained.

For x-rays, the lensless setup becomes a routine way to obtain high resolution phase images. Zone plates are the predominant choice for the objective lens of high-resolution x-ray microscopes. However, the manufacture of narrow outer rings of a zone plate is very challenging and expensive, especially for hard x-rays. The lensless setup of ptychography not only removes the need for lenses and improves the resolution, but also gains the quantitative phase information. Our optical tests here confirm that the use of a diffuser in the probe-forming optics can be highly beneficial for x-ray ptychography (Stockmar *et al.*, 2013; Maiden *et al.*, 2014; Li *et al.*, 2016). It is not practical to adopt the microscope setup and the selected area setup in the x-ray regime because of the poor quality and low numerical aperture of the zone plates.

For electrons, the lensless setup can be implemented on a scanning electron microscope, but a practical difficulty is adjustment of the magnification over a good range with a fixed or marginally adjustable camera length (Humphry *et al.*, 2012). This is avoided by the use of the intermediate lenses in

the transmission electron microscope, where the available options are the microscope setup (Putkunz *et al.*, 2012) and the selected area setup (Maiden *et al.*, 2015). Resolution improvements are not apparent in these two cases, where the primary gain is an effective way to quantify the phase of the electron wave. With recent developments, ptychography can also be implemented in scanning transmission electron microscopy (STEM) and provide quantitative phase information at atomic resolution (Yang *et al.*, 2016).

Acknowledgements

The authors acknowledge the support of the Engineering and Physical Sciences Research Council (EPSRC) through grant no. EP/N019563/1.

References

- Bates, R.H.T. & Rodenburg, J.M. (1989) Sub-Ångström transmission microscopy: a Fourier transform algorithm for microdiffraction plane intensity information. *Ultramicroscopy* **31**, 303–307.
- Brown, H.G., D'Alfonso, A.J., Chen, Z. *et al.* (2016) Structure retrieval with fast electrons using segmented detectors. *Phys. Rev. B* **93**, 1–10.
- Dierolf, M., Menzel, A., Thibault, P. *et al.* (2010) Ptychographic X-ray computed tomography at the nanoscale. *Nature* **467**, 436–439.
- Faulkner, H.M.L. & Rodenburg, J.M. (2004) Movable aperture lensless transmission microscopy: a novel phase retrieval algorithm. *Phys. Rev. Lett.* **93**, 1–4.
- Guizar-Sicairos, M. & Fienup, J.R. (2008) Phase retrieval with transverse translation diversity: a nonlinear optimization approach. *Opt. Express* **16**, 7264–7278.
- Godard, P., Carbone, G., Allain, M. *et al.* (2011) Three-dimensional high-resolution quantitative microscopy of extended crystals. *Nat. Commun.* **2**, 1–6.
- Godden, T.M., Suman, R., Humphry, M.J., Rodenburg, J.M. & Maiden, A.M. (2014) Ptychographic microscope for three-dimensional imaging. *Opt. Express* **22**, 12513–12523.
- Goodman, J.W. (2005) *Introduction to Fourier Optics*. Roberts and Company Publishers, Englewood, Colorado, USA.
- Hoppe, W. (1969a) Diffraction in inhomogeneous primary wave fields. 1. Principle of phase determination from electron diffraction interference. *Acta Crystallogr. A* **25**, 495–501.
- Hoppe, W. & Strube, G. (1969) Diffraction in inhomogeneous primary wave fields. 2. Optical experiments for phase determination of lattice interferences. *Acta Crystallogr. A* **25**, 502–507.
- Hoppe, W. (1969b) Diffraction in inhomogeneous primary wave fields. 3. Amplitude and phase determination for nonperiodic objects. *Acta Crystallogr. A* **25**, 508–515.
- Hegerl, R. & Hoppe, W. (1970) Dynamische Theorie der Kristallstruktur-analyse durch Elektronenbeugung im inhomogenen Primärstrahlwellenfeld. *Ber. Bunsenges. Physik. Chemie.* **74**, 1148–1154.
- Hegerl, R. & Hoppe, W. (1972) Phase evaluation in generalized diffraction (ptychography). *Proc. Fifth Eur. Cong. Electr. Microsc.* 628–629.
- Humphry, M.J., Kraus, B., Hurst, A.C., Maiden, A.M. & Rodenburg, J.M. (2012) Ptychographic electron microscopy using high-angle dark-field scattering for sub-nanometre resolution imaging. *Nat. Commun.* **3**, 730.

- Li, P., Batey, D.J., Edo, T.B., Parsons, A.D., Rau, C. & Rodenburg, J.M. (2016) Multiple mode x-ray ptychography using a lens and a fixed diffuser optic. *J. Opt.* **18**, 1–8.
- McCallum, B.C., Landauer, M.N. & Rodenburg, J.M. (1995) Complex image reconstruction of weak specimens from a three-sector detector in the STEM. *Optik* **101**, 53–62.
- Maiden, A.M. & Rodenburg, J.M. (2009) An improved ptychographical phase retrieval algorithm for diffractive imaging. *Ultramicroscopy* **109**, 1256–1262.
- Maiden, A.M., Humphry, M.J., Sarahan, M.C., Kraus, B. & Rodenburg, J.M. (2012a) An annealing algorithm to correct positioning errors in ptychography. *Ultramicroscopy* **120**, 64–72.
- Maiden, A.M., Humphry, M.J. & Rodenburg, J.M. (2012b) Ptychographic transmission microscopy in three dimensions using a multi-slice approach. *JOSA A* **29**, 1606–1614.
- Maiden, A.M., Rodenburg, J.M. & Humphry, M.J. (2010) A new method of high resolution, quantitative phase scanning microscopy. *Int. Soc. Opt. Photo. Scan. Microsc.* **2010**, 77291I–77291I.
- Maiden, A.M., Sarahan, M.C., Stagg, M.D., Schramm, S.M. & Humphry, M.J. (2015) Quantitative electron phase imaging with high sensitivity and an unlimited field of view. *Sci. Rep.* **5**, 1–8.
- Moore, D.B. & Fienup, J.R. (2016) Ptychography for optical metrology with limited translation knowledge. *Appl. Opt.* **55**, 4596–4610.
- Maiden, A.M., Morrison, G.R., Kaulich, B., Gianoncelli, A. & Rodenburg, J.M. (2014) Soft X-ray spectromicroscopy using ptychography with randomly phased illumination. *Nat. Commun.* **4**, 1–7.
- Putkunz, C.T., D'Alfonso, A.J., Morgan, A.J. *et al.* (2012) Atom-scale ptychographic electron diffractive imaging of boron nitride cones. *Phys. Rev. Lett.* **108**, 1–4.
- Rodenburg, J.M. & Faulkner, H.M. (2004) A phase retrieval algorithm for shifting illumination. *Appl. Phys. Lett.* **85**, 4795–4797.
- Rudin, L.I., Osher, S. & Fatemi, E. (1992). Nonlinear total variation based noise removal algorithms. *Physica D* **60**, 259–268.
- Stockmar, M., Cloetens, P., Zanette, I., Enders, B., Dierolf, M., Pfeiffer, F. & Thibault, P. (2013) Near-field ptychography: phase retrieval for inline holography using a structured illumination. *Sci. Rep.* **3**, 1–6.
- Thibault, P., Dierolf, M., Bunk, O., Menzel, A. & Pfeiffer, F. (2009) Probe retrieval in ptychographic coherent diffractive imaging. *Ultramicroscopy* **109**, 338–343.
- Tripathi, A., McNulty, I. & Shpyrko, O.G. (2014) Ptychographic overlap constraint errors and the limits of their numerical recovery using conjugate gradient descent methods. *Opt. Express* **22**, 1452–1466.
- Thibault, P. & Menzel, A. (2013) Reconstructing state mixtures from diffraction measurements. *Nature* **494**, 68–71.
- Thibault, P., Dierolf, M., Menzel, A., Bunk, O., David, C. & Pfeiffer, F. (2008) High-resolution scanning x-ray diffraction microscopy. *Science* **321**, 379–382.
- Van Heel, M. & Schatz, M. (2005) Fourier shell correlation threshold criteria. *J. Struct. Biol.* **151**, 250–262.
- Yang, H., Pennycook, T.J. & Nellist, P.D. (2015) Efficient phase contrast imaging in STEM using a pixelated detector. Part II: optimisation of imaging conditions. *Ultramicroscopy* **151**, 232–239.
- Yang, H., Rutte, R.N., Jones, L. *et al.* (2016) Simultaneous atomic-resolution electron ptychography and Z-contrast imaging of light and heavy elements in complex nanostructures. *Nat. Commun.* **7**, 1–8.
- Zhang, F., Peterson, I., Vila-Comamala, J. *et al.* (2013) Translation position determination in ptychographic coherent diffraction imaging. *Opt. Express* **21**, 13592–13606.
- Zheng, G., Horstmeyer, R. & Yang, C. (2013) Wide-field, high-resolution Fourier ptychographic microscopy. *Nat. Photo.* **7**, 739–745.